The Astrophysical Journal, 860:47 (12pp), 2018 June 10
https://doi.org/10.3847/1538-4357/aac170

Ionized Gas Motions and the Structure of Feedback near a Forming Globular Cluster in NGC 5253

Daniel P. Cohen[1], Jean L. Turner[1], S. Michelle Consiglio[1], Emily C. Martin[1], and Sara C. Beck[2]
[1] University of California, Los Angeles, CA 90095-1547, USA; dcohen@astro.ucla.edu
[2] School of Physics and Astronomy, Tel Aviv University, Ramat Aviv, Israel
Received 2018 March 2; revised 2018 April 25; accepted 2018 April 26; published 2018 June 11

Abstract

We observed Brackett α 4.05 μm emission toward the supernebula in NGC 5253 with NIRSPEC on Keck II in adaptive optics mode, NIRSPAO, to probe feedback from its exciting embedded super star cluster (SSC). NIRSPEC's Slit-viewing Camera was simultaneously used to image the K-band continuum at $\sim 0\farcs1$ resolution. We register the IR continuum with *HST* imaging, and find that the visible clusters are offset from the K-band peak, which coincides with the Brα peak of the supernebula and its associated molecular cloud. The spectra of the supernebula exhibit Brα emission with a strong, narrow core. The linewidths are 65–76 km s^{-1}, FWHM, comparable to those around individual ultra-compact H II regions within our Galaxy. A weak, broad (FWHM $\simeq$ 150–175 km s^{-1}) component is detected on the base of the line, which could trace a population of sources with high-velocity winds. The core velocity of Brα emission shifts by +13 km s^{-1} from NE to SW across the supernebula, possibly indicating a bipolar outflow from an embedded object or a link to a foreground redshifted gas filament. The results can be explained if the supernebula comprises thousands of ionized wind regions around individual massive stars, stalled in their expansion due to critical radiative cooling and unable to merge to drive a coherent cluster wind. Based on the absence of an outflow with large mass loss, we conclude that feedback is currently ineffective at dispersing gas, and the SSC retains enriched material out of which it may continue to form stars.

Key words: galaxies: dwarf – galaxies: individual (NGC 5253) – galaxies: starburst – galaxies: star clusters: general – galaxies: star formation – H II regions

1. Introduction

Massive star clusters are fundamental components of galactic evolution. Details of gas retention or expulsion during cluster formation must be reconciled with the existence of long-lived massive clusters, globular clusters (GCs), and with multiple stellar populations observed in the GCs (Piotto et al. 2015; Silich & Tenorio-Tagle 2017). Massive clusters contain concentrations of the most massive stars (Kroupa & Boily 2002; Kroupa et al. 2013), whose evolution can potentially induce great radiative, dynamical, and chemical changes in their host galaxies. To probe the formation of GCs, we can utilize observations of local protoglobular cluster candidates, super star clusters (SSCs). They can be as young as ∼1–10 Myr (e.g., Turner 2009).

One of the most thoroughly studied forming GCs is the compact radio/IR nebula, the "supernebula," in the dwarf starburst galaxy NGC 5253. First discovered in the radio from its compact, thermal free–free emission (Beck et al. 1996), this giant H II region (Beck et al. 1996; Calzetti et al. 1997; Turner et al. 1998) is powered by a massive SSC ($M_{\rm vir} = 2.5 \times 10^5\,M_\odot$) with $L \sim 5 \times 10^8\,L_\odot$ and ∼2000 O stars (Turner et al. 2000, 2003, 2017; Meier et al. 2002; Vanzi & Sauvage 2004; Hunt et al. 2005; Calzetti et al. 2015; Smith et al. 2016). The supernebula may be part of the core of a larger star-forming region containing 4000–7000 O stars (Meier et al. 2002). What we refer to as the supernebula is its ∼3 pc core (Turner & Beck 2004; Bendo et al. 2017; Consiglio et al. 2017).

The supernebula is still deeply embedded within its natal cloud—extinction from dust is so high that it is invisible in wavelengths shorter than the NIR, and is the brightest source in the galaxy at wavelengths longer than the H-band (Turner et al. 2003; Alonso-Herrero et al. 2004; Martín-Hernández et al. 2005). Its dustiness ($A_V \gtrsim 16$–18), together with detection of Wolf–Rayet signatures (Conti 1991; Schaerer et al. 1997; López-Sánchez et al. 2007; Monreal-Ibero et al. 2010; Westmoquette et al. 2013), suggest the presence of stars ∼1–3 Myr in age (e.g., Alonso-Herrero et al. 2004; Calzetti et al. 2015; Smith et al. 2016). Submillimeter observations found a warm CO($J = 3$–2) cloud, Cloud "D1," that is coincident to within 0.6 pc of the H II region and within 2 km s^{-1} of IR and radio recombination line (RRL) velocities (Turner et al. 2015, 2017). This gives the first indication that there are potential star-forming molecular clouds within the cluster itself. The CO gas is remarkably quiescent (∼22 km s^{-1} FWHM) considering its extreme environment, within a 3 pc region containing thousands of O stars. The linewidth of Cloud D1 reflects only the gravitational motions of the cluster, with no evidence for molecular outflow. The supernebula thus does not appear to be launching a galactic wind of the kind seen, for example, in NGC 253 (Sakamoto et al. 2006; Bolatto et al. 2013).

Observations of the supernebula suggest feedback is similarly ineffective in driving outflows of ionized gas from the exciting SSC. Turner et al. (2003) observed the Brackett α and γ recombination lines in the supernebula with a $0\farcs5$ slit using NIRSPEC and found, in addition to high extinction, a relatively small linewidth (FWHM of 76 km s^{-1}), similar to widths seen in Galactic H II regions and comparable to the escape velocity of the cluster measurements of mid-IR emission lines (Beck et al. 2012), and RRLs (Rodríguez-Rico et al. 2007; Bendo et al. 2017) confirm this measurement. The gravity of the massive cluster clearly has a large role in shaping the gas motions and could even launch a cluster wind. Numerical wind models suggest that if the NGC 5253 supernebula is sufficiently chemically enriched, strong radiative cooling can suppress a cluster wind (Silich et al. 2003, 2004; Silich & Tenorio-Tagle 2017). Localized chemical enrichment has in fact been indicated in NGC 5253 by nuclear abundance studies (Walsh & Roy 1989; Kobulnicky et al. 1997; López-Sánchez et al. 2007; Monreal-Ibero et al. 2010; Westmoquette et al. 2013) and by submillimeter continuum emission from dust (Turner et al. 2015) and in other SSCs (Consiglio et al. 2016).

In this study, we present high-resolution (0.″1) observations of Br α emission across the NGC 5253 supernebula, made with the NIRSPEC spectrograph on Keck using laser-guided adaptive optics (NIRSPAO). At 4 μm, the Brα line is less effected by extinction than Hα or Br γ. What is happening to the gas in this potential proto-GC, which appears to be in its infant phase? The goal of this investigation is to use our Brα observations to infer the kinematics of the supernebula and determine the influence and fine structure of feedback from the cluster. At the 3.8 Mpc distance of NGC 5253 (Sakai et al. 2004), 0.″1 = 1.8 pc.

2. Observations and Data

The supernebula in NGC 5253 was observed with NIRSPAO on Keck II (McLean et al. 1998) in the second half-night on 2015 May 1. Spectra were taken in high-resolution mode ($R \sim 25{,}000$), in the KL band, using the 2.″26 × 0.″068 slit. The echelle and cross-disperser angles were set to 64.°5 and 34.°12, respectively, yielding a wavelength coverage of roughly 4.03–4.08 μm in the 19th echelle order. The spatial resolution of the observations is ≃0.″12, determined from the continuum spectra of several calibration stars.

The slit was oriented at a position angle of 113.°5 (so that the slit-parallel direction is close to the E–W axis), with each position separated by the slit width (≃0.″07). The slit positions are hereafter labeled: N2, N1, S1, and S2 from north to south. During spectral exposures, the the Slit-viewing Camera (SCAM) was used to simultaneously and continuously image the slit on the sky in the K band, giving a record of the slit position relative to the NIR continuum.

A stacked, reduced SCAM image was constructed to study the spatial distribution of gas and determine registration of slit positions with respect to the radio supernebula. To form this image, raw SCAM images with the supernebula on-slit were subtracted by images taken with the supernebula off-slit (at the end of the night during sky exposures). Then, for each separate slit position, clusters visible in the field of view were used to align all sky-subtracted SCAM images. The slits were masked out in each of the four images, which were then aligned, and the average was computed over each pixel to form a combined, slit-free SCAM image.

To reduce the NIRSPAO spectra, we applied spatial and spectral rectification to all raw NIRSPEC images using the IDL-based REDSPEC pipeline.[3] Arc lamps used for calibration were not functioning properly for the observing run, yielding no emission lines in the Brα order. New arc lamp spectra obtained on a later date (with the same configuration) detect emission lines in this order, but the resulting wavelength calibration is inaccurate in its wavelength zero-point. The issue can be partially corrected by determining the offset between the rest wavelength of Brα and the Brα absorption line detected in a calibrator star spectrum. However, there is no measurement of radial velocity for the calibrator. Centroid velocities inferred from the Brα emission of the supernebula are ∼30–40 km s^{-1} higher than the previously determined velocity of 391 ± 2 km s^{-1} (barycentric), measured for the H30 α line (Bendo et al. 2017) and for the narrow component on the [S IV] 10.5 μm line (Beck et al. 2012). Fortunately, we have He I and Brα lines to determine the wavelength scale, and the measured and expected separation between these lines are consistent to within 2%–3%, or $\lesssim$6 km s^{-1}. Because we are only interested in the velocity linewidths and the relative variation of centroid velocity across the supernebula region, the velocity zero-point does not change any of our results or conclusions. To facilitate comparison with other studies, we shift the spectra so that the Brα in the average spectrum across the four slit positions is at a centroid velocity of 391 km s^{-1}.

Following rectification, individual spectra were sky-subtracted and divided by a median-normalized flat-field image, and hot/cold pixels were removed. Reduced exposures were median-combined to form the 2D spectrum, or echellogram, for each of the four slit positions. Fringe patterns due to interference within the detector are apparent in the echellograms. We tested a correction for fringing but find that it does not significantly change any results or derived quantities. Since these are slit spectra made through AO observations it is difficult to estimate the absolute calibration of line strength, which has been done elsewhere (Turner et al. 2003). The resulting four echellograms have spectral resolution of ∼12 km s^{-1} and spatial resolution of ≃0.″1 (with pixel size 0.″018 pix^{-1} in the spatial direction).

For analysis of kinematics (Section 4), 1D spectra are extracted by summing or averaging rows in the echellograms. Gaussian models are fit to the emission in the extracted spectra to infer line properties.

3. Nature of the NIR Continuum and Relation to Visible Clusters

The NIRSPAO echellograms (spectrum along the x-axis, slit along the y-axis) are shown in Figure 1 along with the positions of the slits, on the stacked SCAM image. The spectra reveal strong Brα emission arising from the supernebula, which is spatially coincident with the 4 μm continuum. Blueward of Brα, there is a detection of the He I 4.04899,4.04901 μm emission line doublet (Hamann & Simon 1986; Tokunaga 2000) from the supernebula. The SCAM imaging, shown in Figure 2, detects K-band continuum associated with the features in the Brα spectra and can be used to provide an astrometric and morphological context for the supernebula.

The Brα line and surrounding 4 μm continuum emission are strongest in slit position S1, confirming that this position is centered closest to the core of the supernebula. Although interpolation between slits to determine an exact peak is nontrivial, the intensity variation implies a Brα peak that is $\lesssim$0.″05 north of the center of the S1 slit. The peak of the brightest K-band source is likewise located between S1 and N1, and coincident with the Brα peak to within half a 0.″07 slit.

The relative positions of the embedded radio/IR supernebula with the optical clusters in the region has been an issue of some debate, since it is clear that there is significant extinction in the region (Calzetti et al. 1997; Turner et al. 2003). The coordinates in *HST* images are not known to subarcsecond precision relative to the International Celestial Reference System (ICRS) coordinates,

---

[3] https://www2.keck.hawaii.edu/inst/nirspec/redspec.html

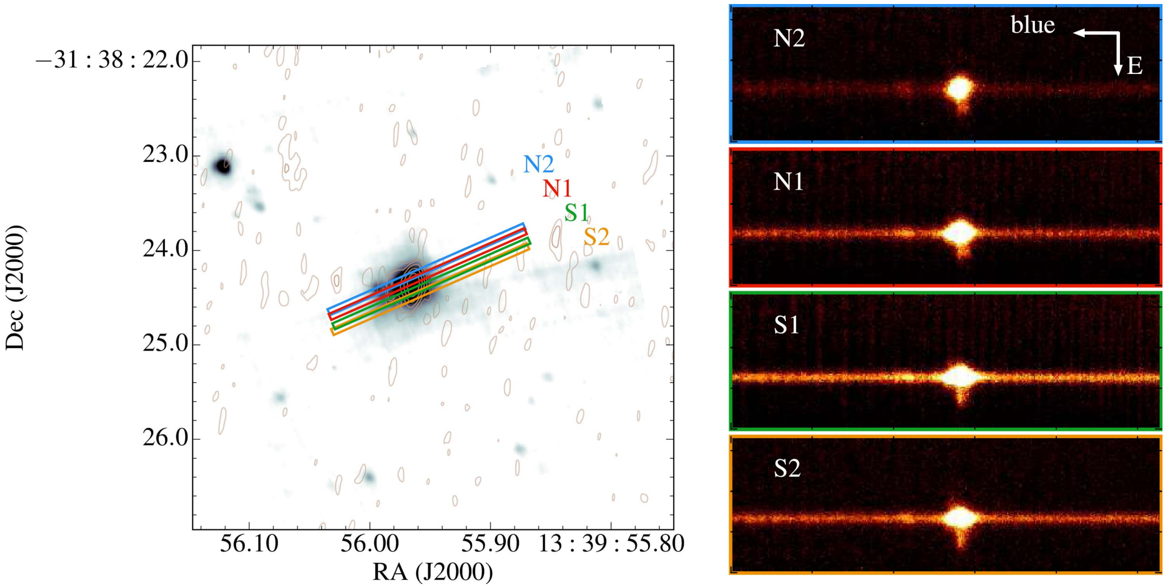

Figure 1. Echellograms of the supernebula in NGC 5253. (Left) K-band continuum from SCAM showing slit positions. Contours show the 1.3 cm continuum map from Turner et al. (2000), which traces free–free radiation. (Right) In each spectrum, east runs vertically downward, and the spectral direction runs horizontally with wavelength increasing to the right. The spectra show (i) strong Brα emission and continuum from the supernebula, (ii) weaker He I emission from the supernebula, and (iii) an extension of Brα emission primarily to the east of the supernebula's continuum (extending down in the figure); $0.''1 = 1.8$ pc.

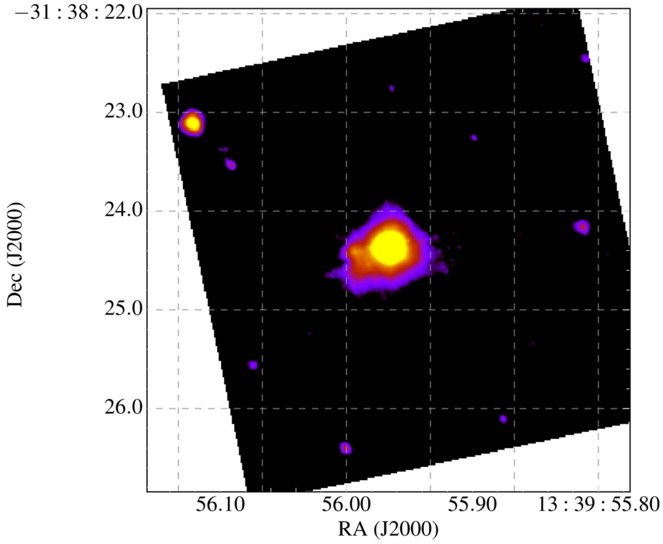

Figure 2. K-band continuum of the supernebula and surrounding clusters. The slit-free, stacked SCAM image, with resolution $\simeq 0.''1$, is shown here in log scale to highlight extended features. The size of the supernebula core is $0.''2$ FWHM in this image, derived from a Gaussian fit to the emission profile. A secondary K-band peak is detected $\simeq 0.''4$ east of the peak emission of the supernebula.

which are determined to $\lesssim$50 mas coordinates in the VLA and ALMA images of the free–free and CO(3–2) emission: $(\alpha,\ \delta)_{\rm 7mm} = (13^{\rm h}39^{\rm m}55^{\rm s}\!.9631,\ 31^\circ38'24''\!.388)$ (Turner & Beck 2004) and $(\alpha,\ \delta)_{\rm CO} = (13^{\rm h}39^{\rm m}55^{\rm s}\!.9561,\ 31^\circ38'24''\!.364)$ (Turner et al. 2017). Our new AO view of the region's NIR continuum from SCAM taken simultaneously with the Br α can now tell us how the visible light and IR-radio light within the vicinity of the supernebula are related by linking the K-band peak, hence the bright Brα source, to the optical clusters.

Registration of the SCAM and *HST* images is determined by aligning the bright NIR clusters in the SCAM images (some of these clusters can be seen in Figure 2), with optical counterparts in the *HST* F814W image from the LEGUS survey (Calzetti et al. 2015). Registration of the SCAM and radio images is determined by noting that the bright free–free source in the radio images is the same source responsible for the brightest Brα emission, which we have found is coincident with the K-band peak. We can then align the *HST* images with the VLA and ALMA images to within ∼50 mas. This registration is reinforced by visually aligning these registered *HST* images with bright clumps in the CO map of Turner et al. (2017); the bright CO peak associated with Cloud D1 is coincident with the supernebula and Br α peak. Aligned this way, the CO clouds coincide with regions of visual extinction.

In Figure 3, we overlay the registered slit-free SCAM image with the *HST* F814W image and the ALMA CO(3–2) map. Here we identify visible clusters #5 and #11 from Calzetti et al. (2015) and cluster #105 from de Grijs et al. (2013). Clusters #5 and #11 possibly contain stars with ages of $\lesssim$1 Myr, based on radio fluxes and SED modeling by Calzetti et al. (2015), who suggest that these visible point-like sources could be the SSCs that power the supernebula. As seen in Figure 3, these clusters are not coincident with the K-band/Brα peak emission of the supernebula: cluster #5 is offset by $0.''35$ or 6.4 pc, while cluster #11 is closer to $0.''14$ or 2.6 pc. The compact radio core of the supernebula (Turner & Beck 2004) requires an extremely luminous cluster—even the small offset of cluster #5 to the edge of the nebula would introduce a solid angle-induced luminosity augmentation that is inconsistent with the already "too large" cluster luminosity, given the dynamical mass constraints imposed by the CO linewidth (Turner et al. 2017).

The perfect coincidence of the NIR continuum peak with the compact radio supernebula and Cloud D1, its extended appearance, and correspondence with the visible extinction, imply that the 2 μm continuum is from dust emission. The presence of localized dust in the supernebula is supported by the detection of strong submillimeter continuum, indicating a substantial ($10^{4.2}\,M_\odot$) amount of dust (Turner et al. 2015). If

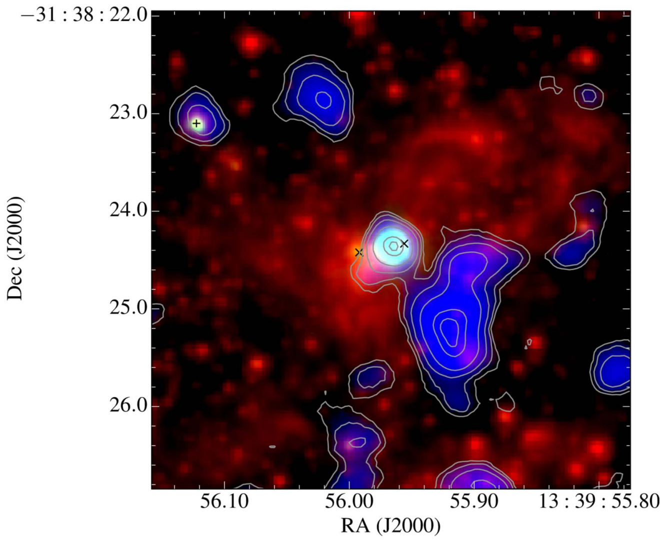

Figure 3. Overlay of the K-band continuum, optical, and CO emission near the supernebula. The SCAM K-band image is in green, the F814W continuum from *HST*/LEGUS (Calzetti et al. 2015) is in red, and ALMA CO(3–2) is shown in blue and with contours (Turner et al. 2017). The coincidence of the NIR continuum with the CO cloud D1 and visible extinction causes the embedded supernebula to appear light blue. Positions of visible clusters near the supernebula from Calzetti et al. (2015) are shown as black X's: clusters #5 and #11 are offset 0.″35 east and 0.″14 west of the supernebula peak, respectively. Cluster 105 from de Grijs et al. (2013) is shown with a black cross. Positions of the optical clusters have been shifted based on radio registration as described in the text.

even a small fraction of this dust is at temperatures of $T_d \sim 750$ K, the emission is easily explained. Furthermore, there is excess NIR flux from the supernebula that cannot be accounted for by purely stellar+nebular models, requiring a dust emission component (Alonso-Herrero et al. 2004; Calzetti et al. 2015). The extended nature of the K-band emission, with a size of 0.″2 FWHM = 3.7 pc, suggests that the hot dust is not concentrated in the core of the supernebula cluster, especially if the eastern component (near cluster #5) is also from dust.

Although offset east from the supernebula core, cluster #5 is coincident with a weaker, secondary K-band peak detected with SCAM, apparent in Figure 2. This source has also been detected in VLA radio continuum images (Turner et al. 2000). The NIR continuum emission around this component is extended out to ~0.″3 south from its peak. Brα is also detected from the eastern component, seen in Figure 1 as a tail of emission extending out to ~0.″6 or 12 pc to the east of the supernebula peak (well past the position of cluster #5). Such extended morphology calls into question whether this NIR source is indeed starlight from a cluster, or, like the supernebula K-band source, has a significant contribution from hot dust.

In summary, our high-resolution images and spectra reveal no visible clusters at the center of the supernebula that are likely to be the origin of the exciting UV photons. A strong dust continuum at 2 μm can affect inferred properties of the SSC that rely on NIR emission lines and continuum, as noted by Calzetti et al. (2015). Specifically, measurements of age based on the equivalent widths of NIR recombination lines such as Brγ become upper limits, since the contribution to the continuum from the older nonionizing population will be overestimated. Thus, our observations are consistent with previous suggestions the radiation fields powering the radio/IR supernebula are due to very young stars, of age $\lesssim$1–2 Myr (Calzetti et al. 2015; Smith et al. 2016).

4. Brackett α Spectroscopy of the Supernebula

The Brα line profile and its spatial variation encode detailed gas motions, from which we can infer the presence of feedback and how it is affecting the SSC formation. Although we focus on the Brα line, the He I 4.04899,4.04901 μm emission present in the spectra represents the first detection of this doublet in an extragalactic source, to the best of our knowledge. Other He I lines have been observed in the supernebula at visible and NIR wavelengths (Cresci et al. 2010; Smith et al. 2016), indicative of massive exciting stars with high effective temperatures and sizeable He$^+$ zones. The echellograms suggest that the He I emission is more confined to the nebular core than the Brα.

To study the detailed line profile of Brα and its variation between slit positions (Sections 4.1 and 4.2.1), we first analyze integrated spectra, which are extracted by summing 12 rows = 0.″215 in each echellogram centered on the peak Brα emission. The extraction box is chosen to be wide enough to detect faint features but small enough to probe emission from the core, matching the K-band size of the supernebula (Section 3). The signal-to-noise at the line peak in these spectra is estimated from the rms, which includes fringing: $(S/N)_{\rm peak} = 67$, 45, 42, and 43 for slits N1, S1, N2, and S2 respectively. We follow our analysis of integrated spectra with investigation of the more detailed spatial variation of Brα velocity as probed by a map of the emission, extracted by averaging spectra in bins of 6 rows = 0.″108 across each echellogram (Sections 4.2.2 and 4.3).

4.1. The Recombination Line Profile

The Brα emission detected for the four slit positions across the supernebula spans a range of just over 10 km s^{-1} in centroid velocity (about one resolution element of NIRSPEC) and exhibits linewidths of FWHM = 75–87 km s^{-1} (Table 1), based on best-fit models of a single-Gaussian profile to emission at >10% of the line peak intensity (Figure 4). The profile is narrower in the northern slit positions (N1 and N2), comparable with the Brα linewidth of 76 ± 1 km s^{-1} presented in Turner et al. (2003). In slits S1 (closest to the peak of the supernebula) and S2, however, the line is broader by ~10 km s^{-1}. This can be compared to lower spatial resolution RRLs, with FWHMs of 58 ± 12 km s^{-1} for H53α (Rodríguez-Rico et al. 2007) for a 3″ beam, and 68 ± 3 km s^{-1} for H30α (Bendo et al. 2017) for a 0.″2 beam. In the MIR, Beck et al. (2012) inferred a linewidth of 65 km s^{-1} for the [S IV] 10.5 μm emission within a 1.″2 slit.

Figure 4 shows that our high-S/N spectra detect wings on the base of the Brα line at ~10%–15% of the peak line intensity, which cannot be fit well by a single-Gaussian model. To account for this feature, the Brα profiles are additionally fit with a model consisting of two Gaussians: a weak, broad component and a stronger, narrow core. The resulting best-fit parameters are reported in Table 1. The two-component model, shown in Figure 5, provides a better fit in the wings and core of the observed Brα line, suppressing the residuals that result from the single-Gaussian fits. The narrow Brα component is found to have $\mathrm{FWHM_{core}} = 65$–76 km s^{-1}, smaller than the linewidths from the single-Gaussian models, and consistent with previous recombination line measurements, which did not

Table 1
Brα and He I Line Properties from NIRSPAO Spectra for Each Slit Position ($0\farcs2$ Extraction Box)

Slit Position	$v_{\mathrm{Br}\alpha}$ (km s^{-1})[a]	FWHM$_{\mathrm{Br}\alpha}$ (km s^{-1})[b]	$v_{\mathrm{He\,I}}$ (km s^{-1})[c]	FWHM$_{\mathrm{He\,I}}$ (km s^{-1})[d]	$I_{\mathrm{Br}\alpha}/I_{\mathrm{He\,I}}$[e]
avg	391 ± 1	84 ± 1	382 ± 3	81 ± 10	16 ± 1
N2	384 ± 1	75 ± 1	374 ± 4	67 ± 11	15 ± 2
N1	386 ± 1	80 ± 1	380 ± 3	82 ± 8	17 ± 1
S1	394 ± 1	87 ± 1	386 ± 5	86 ± 12	17 ± 2
S2	396 ± 1	86 ± 1	387 ± 4	77 ± 10	14 ± 1

v_{core} (km s^{-1})[f]	FWHM$_{\mathrm{core}}$ (km s^{-1})[g]	v_{wing} (km s^{-1})[h]	FWHM$_{\mathrm{wing}}$ (km s^{-1})[i]	$I_{\mathrm{wing}}/I_{\mathrm{core}}$[j]
391 ± 1	77 ± 1	385 ± 5	189 ± 18	0.13 ± 0.03
384 ± 1	65 ± 2	386 ± 3	147 ± 13	0.22 ± 0.05
386 ± 1	73 ± 1	385 ± 3	177 ± 12	0.15 ± 0.02
395 ± 1	76 ± 2	385 ± 5	163 ± 15	0.20 ± 0.05
397 ± 1	74 ± 2	383 ± 5	154 ± 12	0.23 ± 0.06

Notes. Brα Fit parameters are quoted both for the single-Gaussian model and the two-component model consisting of a strong, narrow core and weak, broad wings.

[a] Centroid velocity (barycentric) of the Brα line (from single fit). A wavelength shift was applied to the spectra so that the Brα emission is at a velocity of 391 km s^{-1} in the average spectrum across the four slit positions, to match the velocity determined from H30α in a $0\farcs2$ beam.

[b] FWHM of Brα emission (from a single-Gaussian fit).

[c] Centroid velocity (heliocentric) of the He I line. The velocity offset of about -10 km s^{-1} for He I relative to Brα could reflect our use of 4.049 μm as the He I rest wavelength, while in reality the line is a blended doublet.

[d] FWHM of the blended He I doublet.

[e] Intensity ratio of Brα to He I.

[f] Centroid velocity of the narrow Brα component.

[g] FWHM of the narrow Brα component.

[h] Centroid velocity of broad Brα component.

[i] FWHM of the broad Brα component.

[j] Peak intensity ratio of broad wings to the core.

detect broad shoulders. We discuss the implications of the Brα linewidths in Section 5.

In the context of cluster feedback, the high-velocity shoulders on the base of the Brα emission line are very intriguing. Our two-component models suggest broad-component widths of FWHM$_{\mathrm{wing}} \simeq 150$–$175$ km s^{-1}. Broad components with FWHM $\simeq 100$–250 km s^{-1} have been detected on the Hα line in the supernebula region, but on a larger scale and for an extended gas component that is much less extincted than the supernebula gas (Monreal-Ibero et al. 2010; Westmoquette et al. 2013). The Brα wings are roughly symmetric about the core in slits N1 and N2, but appear to be stronger on the blue side for slits S1 and S2, supported by a slight blueward shift in the broad-component centroid in S1/S2 relative to N1/N2 (Figure 5 and Table 1). The [S IV] emission from the supernebula exhibits excess emission extending on the blue side out to -100 km s^{-1} from the peak (Beck et al. 2012), suggesting that the slit used for these TEXES observations could have been positioned south of the supernebula peak. However, the discrepancy in velocity is significant: a blue wing is clearly detected for the [S IV] line and extends to high velocity, while the Brα wings are weak and more confined in velocity. Nonetheless, a broad pedestal of emission appears to be a common feature for ionized gas lines in SSCs, previously observed in the Brackett lines from clusters in He 2–10 and other systems (e.g., Henry et al. 2007). As discussed in Section 5, this feature could reflect a population of individual young stellar objects (YSOs) with broad-line profiles or other stars that are driving high-velocity winds (Beck 2008).

4.2. Velocity Structure of the Supernebula

The spatial variation of Brα emission, particularly its centroid velocity, traces the motions of gas associated with the supernebula. We can analyze the velocity structure and determine if it supports a consistent scenario to that implied by the integrated line profile.

4.2.1. North–South Velocity Shift

The centroid velocity of the supernebula core (Table 1) exhibits a clear shift from northern to southern slit positions, shown in the left panel of Figure 6. The magnitude of this shift is $+13$ km s^{-1} across the $\sim 0\farcs3 = 5.5$ pc between N2 and S2; about one full resolution element of NIRSPEC. Subtraction between the southern and northern echellograms, shown in the right panel of Figure 6, supports the Brα core shift inferred from the 1D spectra. The most intriguing feature in this figure is the negative arc that curls around the blue side of the southern Brα peak. This profile results from the line core shift to the blue of the northern portion, and because the northern emission is more spatially extended than the southern portion. Indeed, the intensity profiles along each slit indicate that the Brα emission is more extended by $\sim 0\farcs15$ in N2 relative to that in S2. Similar velocity structure is suggested by the H53α line, which exhibits a NW–SE gradient of 10 km s^{-1} arcsec^{-1} on much larger ($3''$) scales (Rodríguez-Rico et al. 2007), along with channel maps of the H30α line, which reveal blueshifted emission in the NE edge of the supernebula (Bendo et al. 2017). To the south of the supernebula/Cloud D1, there is another CO cloud, D4, that is redshifted relative to D1 (Consiglio et al. 2017). The CO(3–2) morphology suggests a potential connection between D1 and D4 (Figure 3), which could explain the Brα velocity shift. Alternatively the Brα gradient could indicate cluster rotation, or an outflow with a bipolar morphology. We discuss these possibilities in Section 5.

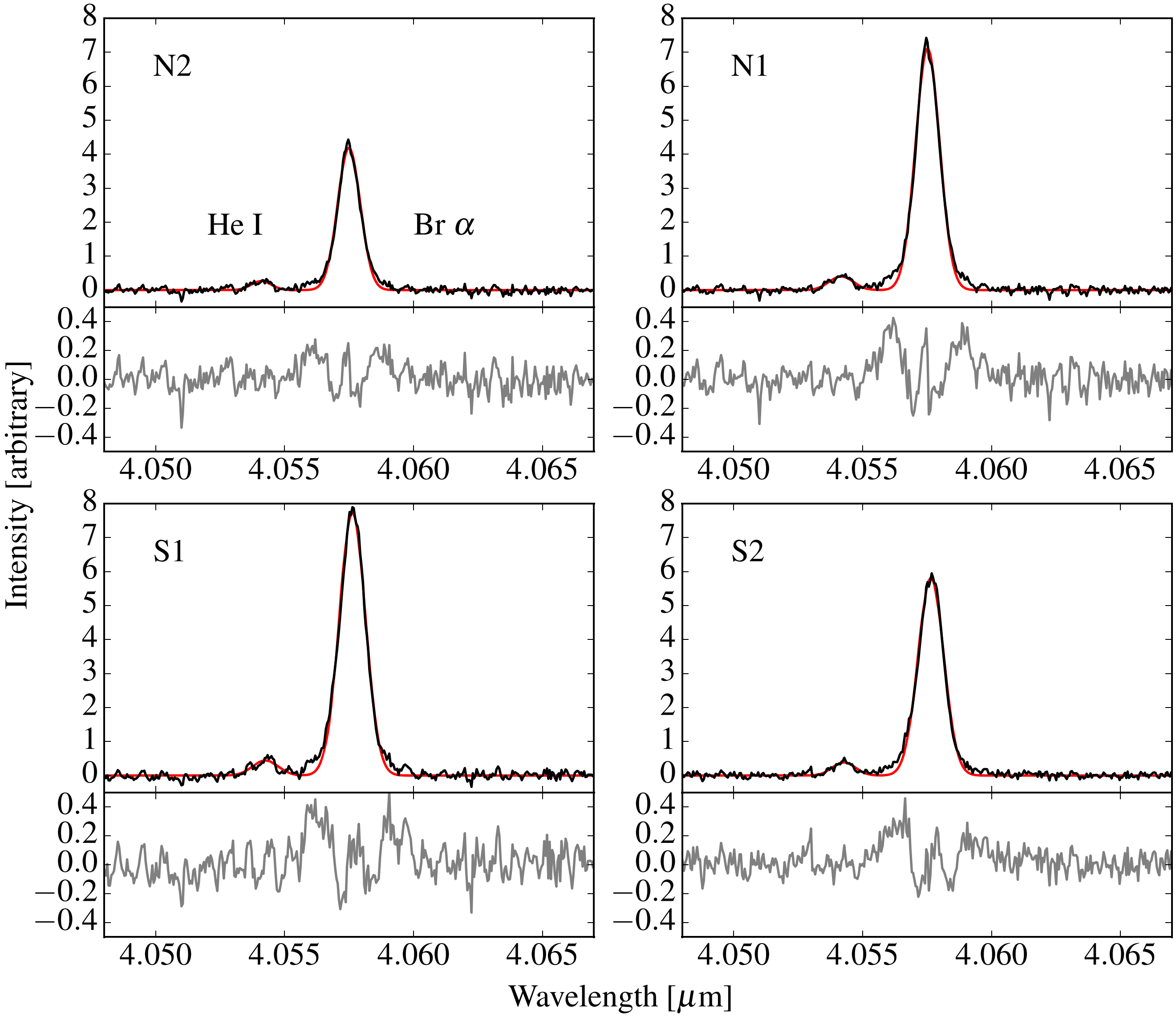

Figure 4. Continuum-subtracted, 1D spectrum extracted with a $0\farcs2$ aperture from the echellograms for each of the four slit positions. For each spectrum, the top panel shows the data (black curve) and best-fit models of single-Gaussian profiles for the Brα and He I lines (red curve), and the bottom panel shows the fit residual's data −model (gray curve). We only fit Brα emission at above 10% of the line peak to account for faint wings.

The velocity shifts described above apply to the narrow line core, the strongest portion of the Brα, but not necessarily to the broad component of the line described in Section 4.1. As indicated in Figure 5, the Brα wings are more apparent on the blue side of the line for slits S1 and S2. This could result from a slight blueshift in the velocity centroid of the broad emission from north to south, although the Gaussian fits suggest that the broad component is static across the supernebula (Figure 6). Alternatively, there could be an asymmetry of the broad component in the south, possibly owing to extinction effects or inherent variance between the populations of broad-line sources contained in each slit. That there are still features present in the residuals of Figure 5 supports such an asymmetry. Ultimately, more sensitive observations of the Brα wings are required to study their variation near the cluster.

4.2.2. 2D Variation in Line Core Velocity

Figure 7 shows the map of the Brα spectrum in $\sim 0\farcs1$ bins across the full $\gtrsim 1''$ extent of emission. The map reveals the changes in line profile across the region. The centroid velocity of Brα is inferred with best-fit single-component Gaussian models to each spectrum within the map.

The Brα map provides a more detailed picture of the velocity structure near the supernebula, including variations of the emission parallel to the slits. Figure 8 shows the Brα centroid as a function of position along the slit, for each of the four slits. This plot recovers the blueshift of emission in slits N1/N2 relative to that in S1/S2, within the extent of the supernebula. Moreover, for a given slit, there is a velocity shift from the edges toward the center of the supernebula, with the northern emission being blueshifted in the center relative to the edges, while the southern emission is redshifted. This structure further disfavors spherically symmetric expansion of the ionized gas.

The full 2D velocity structure is visualized in the context of the K-band continuum (Section 3) in Figure 9, which overlays filled contours of centroid velocity on the SCAM image and its intensity contours (akin to a moment-one map). The NE–SW velocity gradient across the supernebula represents the only

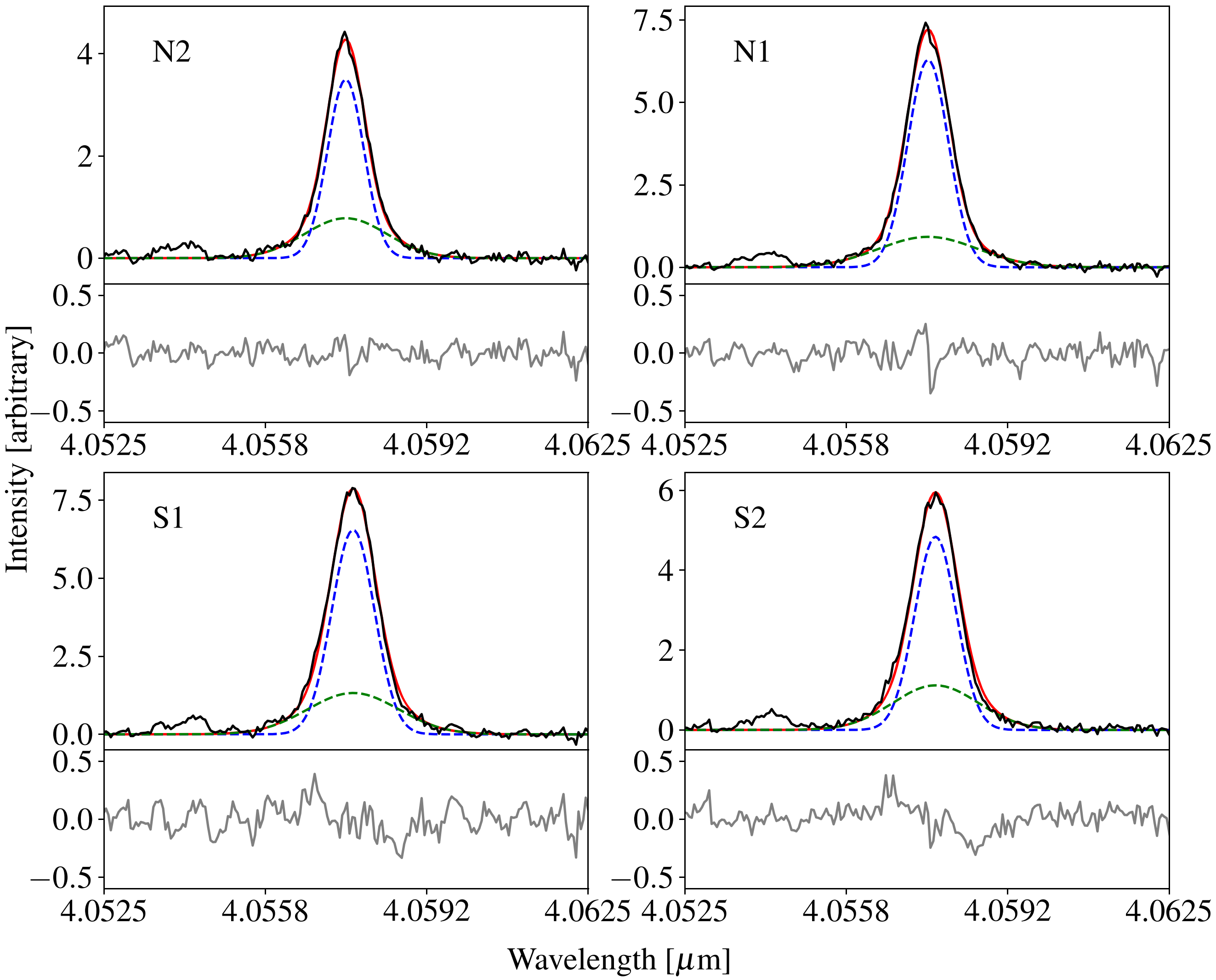

Figure 5. Same as in Figure 4, except the Brα is fit with a two-component Gaussian model: a weak, broad component (dashed green line) for the shoulders at the base of the line, and a stronger, narrower component corresponding to the line core emission (dashed blue). The combined fit is in red. The two-component model yields smaller residuals (compared with Figure 4) in both the wings and the very core of the line.

potential detected signature of an outflow from the cluster, aside from the broad wings on the Brα line (see Section 5).

4.3. Extended Emission

The NIRSPAO spectra (Figure 1) show that the Brα emission extends $\gtrsim$10 pc (projected) to the SE of the supernebula's peak, well past the core radius. As shown in Section 3, the eastern Brα emission is detected in the K-band imaging as a secondary peak that is coincident with the position of visible cluster #5, surrounded by a more diffuse continuum. As is apparent in Figure 9, gas from the eastern component is redshifted by $\sim$5–15 km s^{-1} relative to the eastern edge of the supernebula, easily distinguished from the supernebula emission region. The maximal redshift in the Brα line of $\sim$10 km s^{-1} relative to the supernebula core is directly associated with the eastern K-band peak/cluster #5. The velocity exhibits a smooth decrease with distance away from the eastern emission peak. That the eastern component is redshifted and has much lower extinction relative to the supernebula suggests that it is on the near side of the supernebula and infalling, with the more compact emission region (cluster #5) leaving behind a wake of gas. Whether or not the gas in the east is related to gas in the south, which is also redshifted (Section 4.2.1), is unclear. Previous observations have found evidence for NW–SE velocity variations near the supernebula. Channel maps of H53α support the presence of redshifted gas extending east from the supernebula, although the lower resolution cannot separate the eastern component from the supernebula (Rodríguez-Rico et al. 2007). Furthermore, ALMA observations of CO(3–2) and CO(2–1) reveal a tail of molecular gas extending east from Cloud D1 on the red side of the line (Turner et al. 2017). In the optical, a NW–SE velocity gradient is measured for a broad component and weaker narrow component of Hα, but with opposite orientation, such that gas is blueshifted to the east (Monreal-Ibero et al. 2010; Westmoquette et al. 2013). However, the Hα is from gas associated with the optical lobes running SE-NW (Figure 3), on scales much larger than the supernebula, while the bright Brα is from heavily reddened gas associated directly with the supernebula. Moreover, the Hα velocity gradient is most apparent for the broad component of Hα, while we only detect velocity structure for the narrow component of Brα. The Hα structure is potentially a signature of an accelerating outflow (Westmoquette et al. 2013); a comparison with

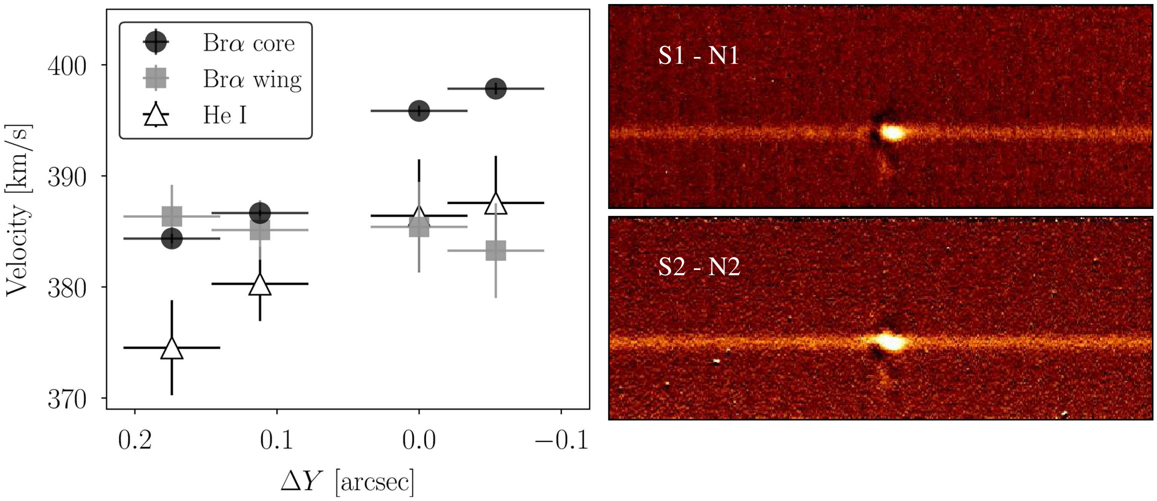

Figure 6. Velocity shift across the supernebula. (Left) Centroid velocity (heliocentric) of the Brα line (narrow and broad components) and He I doublet as a function of slit position in the slit-offset direction; north is left and south is right, and the zero-point is set to slit position S1. There is a clear blueshift of the Brα core and He I doublet in the northern slit positions relative to southern by $\simeq$13 km s^{-1}. We note that He I centroids are offset blueward of Brα; this likely arises from use of a single reference wavelength to derive the velocity of the He I doublet. (Right) Difference between southern (S1/S2) and northern (N1/N2) echellograms The negative arc curling around the blue side of the supernebula's Brα emission is due to the N-S line core shift along with the emission in the north being more extended relative to that in the south.

velocity structure for the Brα wings would be informative but requires more sensitive observations.

5. The Fine Structure of Feedback in NGC 5253

With recent subarcsecond observations, including those we present here for the ionized gas, and for the CO and ionized gas from ALMA (Bendo et al. 2017; Consiglio et al. 2017; Turner et al. 2017), we can begin to understand the physical mechanisms occurring at the subcluster scale in the forming SSC in NGC 5253.

Our NIRSPAO observations reveal a recombination linewidth of 65–76 km s^{-1} (FWHM) in the core, and with a broad component of linewidth ~150–175 FWHM. The broad component is weaker, constituting ~25%–30% of the total line flux. The core emission is relatively narrow, considering that it is convolved both with the H I thermal linewidth of 22–23 km s^{-1}, corresponding to an H II region temperature of 11,000–12,000 K (Kobulnicky et al. 1997), and the dynamical linewidth due to the cluster mass, also 21.7 km s^{-1}. The deconvolved linewidth of ~58–70 km s^{-1} is comparable to the linewidths of individual recombination lines in individual Galactic H II regions (e.g., Jaffe & Martín-Pintado 1999; De Pree et al. 2004; Sewilo et al. 2004; De Pree et al. 2011).

5.1. The Supernebula As a Compact H II Region

Feedback from H II regions can be effective at disrupting GMCs and regulating star formation, depending on the details of their dynamical evolution and interaction with the winds from their exciting massive stars (e.g., Matzner 2002). The simplest model of H II region evolution, spherically symmetric pressure-driven expansion, cannot account for the large number of ultra-compact H II regions (UCHIIs) found embedded within massive-cluster forming regions in the Milky Way, such as in W49 (e.g., Dreher et al. 1984; De Pree et al. 2000).

Realistic models of H II region dynamics solve this well-known "lifetime problem" (e.g., Wood & Churchwell 1989) by invoking dense, molecular gas that can prolong the expansion of the ionized region out of its compact phase. For example, "champagne flows" from blister H II regions can account for much of the observed population of UCHIIs and their morphology (Tenorio-Tagle 1979). Models that can additionally explain the broad recombination lines observed for a large fraction of the UCH II population invoke photoevaporation of circumstellar disks (e.g., Hollenbach et al. 1994; Lizano et al. 1996) or mass-loading of O star winds by photoevaporation of circumstellar clumps (Dyson et al. 1995). The Brα linewidth may seem small considering the extreme cluster luminosity and youth, as noted previously (Turner et al. 2003; Rodríguez-Rico et al. 2007; Beck et al. 2012; Bendo et al. 2017). However, if the supernebula comprises thousands of compact H II regions within the cluster, the line is perfectly consistent with the line profile of an individual compact H II region convolved with the thermal linewidth of H I and the gravitational linewidth of the cluster (Turner et al. 2017), as first pointed out by Beck (2008).

Molecular gas, traced by CO, is present in the NGC 5253 SSC (Turner et al. 2015, 2017; Consiglio et al. 2017). The small CO linewidth, only tracing the stellar motions due to gravity, suggests that the molecular gas is bound to individual stars. Thus, we suggest that the embedded SSC contains thousands of massive stars that are currently accreting in the form of large molecular disks, or heating molecular clumps. These O stars ionize surrounding gas and form compact H II regions, much like Galactic H II regions, which can be sustained at their sizes of ~0.1 pc for the cluster age (~1 Myr or less) through the replenishment of the expanding plasma via photoevaporation and ablation of the bound molecular gas. As discussed further in Section 5.2, radiative cooling is likely to play a fundamental role in preventing the ionized wind regions from merging, and can result in the formation of enriched molecular clumps. The narrow Brα component suggests that most of the H II regions in the SSC are expanding slowly, similar to Galactic H II regions. However, the broad pedestal on the base of the Brα line provides a potential channel for gas escape, with linewidths that are similar to those observed around individual YSOs, which exhibit $\mathrm{FWHM}_{\mathrm{Br}\alpha} = 50$–$250\ \mathrm{km\ s^{-1}}$ (Persson et al. 1984). Despite potential high-velocity winds that could be breaking

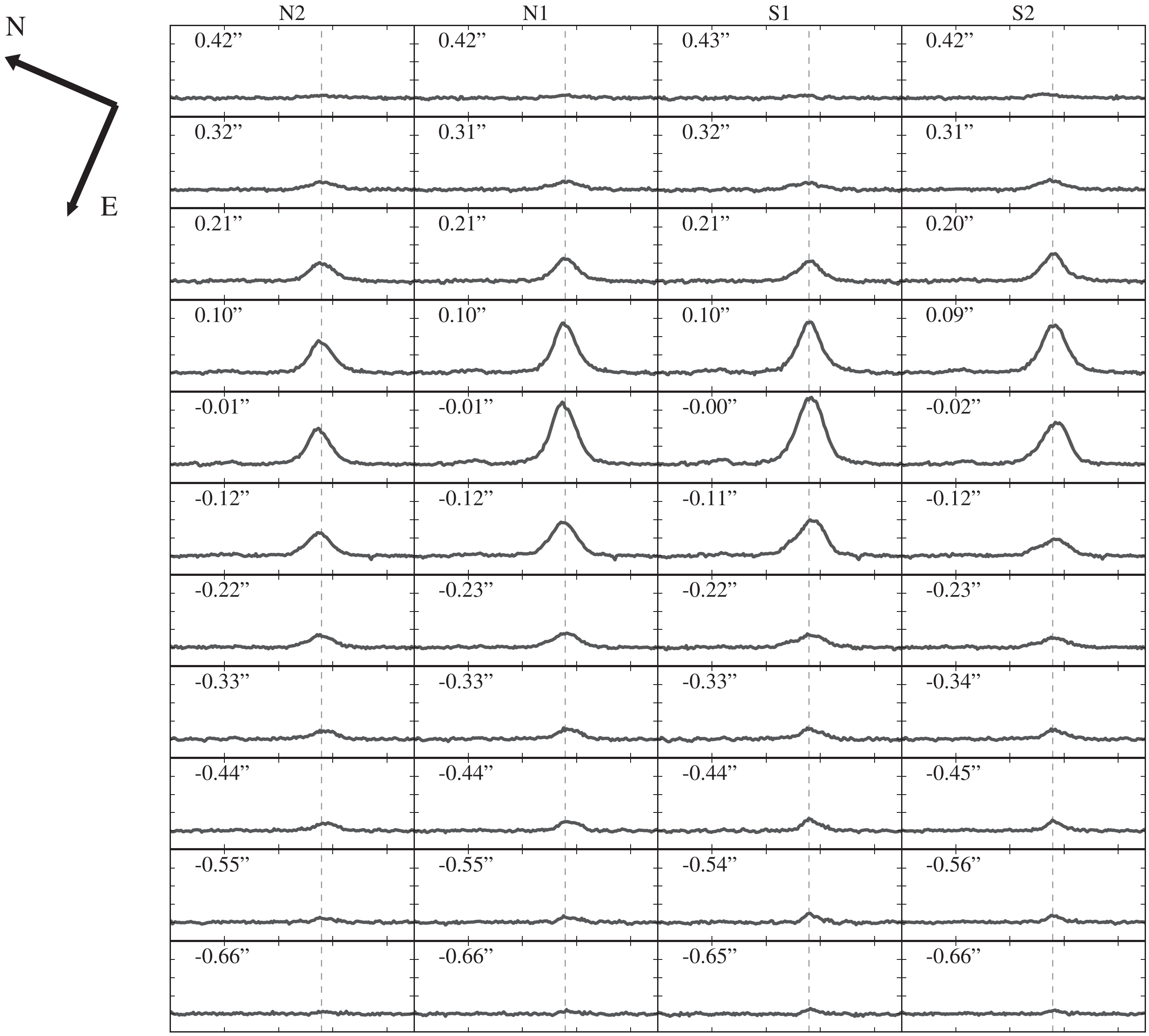

Figure 7. Map of the Brα line across the supernebula, extracted in bins of $\simeq 0\farcs11$ across each echellogram. Each column is a separate slit position, running north to south from left to right, and rows are such that east is down and west is up. For reference, we mark the Brα centroid derived for the average of all four echellograms as a dashed vertical line in each plot. Within each panel, we quote the distance from the peak Brα emission for the corresponding echellogram.

out of the cluster, these broad-line sources contain a small fraction of the cluster’s gas, and are not likely to drive a mass-loss rate that is presently large enough to disrupt the SSC. Nonetheless, the cluster might still influence its environment through these sources by losing mass and thereby polluting the surroundings with enriched material.

5.2. The Suppression of Winds

The details of how a forming cluster disperses its gas shape its evolution and survival. Gas is expelled through winds and supernova explosions (SNe) from massive stars, and the structure and evolution of these outflows are determined by the competing effects of the outward overpressure of thermalized gas, the inwardly directed collective gravity, and energy losses due to radiative cooling. Simulations of feedback-driven winds typically assume the winds are adiabatic, where cooling is negligible. In this case, stellar winds and SNe can merge to form a coherent cluster wind, clearing all gas from an SSC soon after the formation of massive stars (e.g., Chevalier & Clegg 1985; Cantó et al. 2000). In reality, radiative cooling plays a fundamental role in the operation of mechanical feedback and will substantially alter this scenario. Cooling losses are enhanced in chemically enriched gas, and there is strong evidence that the SSC in the NGC 5253 cluster has enriched its environment with products of stellar evolution (Walsh & Roy 1989; Kobulnicky et al. 1997; Schaerer et al. 1997; Monreal-Ibero et al. 2010; Westmoquette et al. 2013; Turner et al. 2015). Our K-band imaging (Section 3) likely traces hot dust emission, localized to the supernebula and extended up to $\lesssim 10$ pc to its east. Based on numerical simulations, Silich et al. (2004) conclude that if the gas metallicity in the supernebula is enhanced to 1.5 $Z_{\odot}$, winds can be entirely inhibited by cooling. Turner et al. (2015) estimate that the metallicity of cloud D1 is the $\simeq$2–3 $Z_{\odot}$, indicating that the SSC is near or above the critical cooling regime. Recent

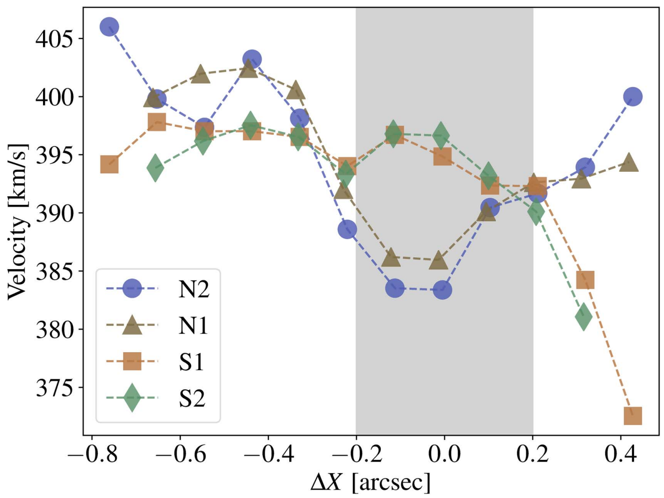

Figure 8. Centroid Brα velocity (heliocentric) vs. position along the slit, showing the E–W velocity variation; east is left and west is right. The zero-point defines the position of the Brα peak along each slit. The supernebula is shaded in gray.

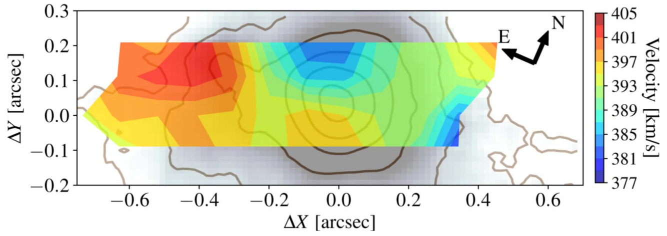

Figure 9. Map of the Brα velocity centroid (heliocentric) near the supernebula. The velocity map is visualized as colored, filled contours, which are overlayed on the SCAM K-band image shown in grayscale and as brown solid contours. This figure shows the correspondence between the gas kinematics and the morphology of the supernebula. ΔX is the slit-parallel direction, with zero-point defined by the peak emission in the echellograms, and ΔY is the slit-perpendicular position, with zero-point defined by the center of slit S1. To overlay the SCAM image, we match the K-band peak to the origin of these axes.

modeling of cluster formation find that in the most massive and dense clusters, stellar winds and even SNe around individual stars can potentially stall due to radiative cooling, and fail to merge with their neighbors (Tenorio-Tagle et al. 2013, 2015; Silich & Tenorio-Tagle 2017; Wünsch et al. 2017; Silich & Tenorio-Tagle 2018). Our Brα observations, suggesting that the supernebula comprises thousands of individual H II regions rather than a single, merged giant H II region, is consistent with critically radiative winds/SNe around the SSC's massive stars. Indeed, NGC 5253 is in the critical density regime defined in Silich & Tenorio-Tagle (2017) in which it will retain its enriched stellar products due to wind stalling. The stalling mechanism can explain the apparent lack of SNe signatures in the SSC without requiring an extremely young cluster age. Another massive embedded SSC, Mrk 71-A (in the dwarf starburst galaxy NGC 2366), is similarly found to exhibit no signs of a cluster-scale outflow or superwind (Oey et al. 2017). This cluster is analogous to NGC 5253, with a mass of $M \sim 10^5\,M_\odot$ and an age of $\lesssim$3 Myr. Whether the suppression of winds, and resulting gas retention, is standard for the most massive clusters, or whether there are other key factors such as host galaxy environment, remains a vital question in our understanding of cluster formation. The ability of the embedded SSC in NGC 5253 to hold onto its gas, even gas enriched through stellar evolution, has significant implications for the cluster's survival and potential evolution into GC. For one, continued formation of stars out of enriched material will lead to a spread in age and abundance in the stellar population, analogous to the multiple stellar populations inferred for many GCs (e.g., Renzini 2013; Piotto et al. 2015, and references therein). Moreover, the suppression of winds forces a slow expulsion of gas, preventing explosive dispersal. Removal of gas from the SSC could occur on a timescale much longer than the crossing time, allowing the cluster to respond adiabatically to changes in the gravitational potential. Along with a high star formation efficiency SFE $\gtrsim$ 50% (Turner et al. 2015), the long gas removal timescale should allow the SSC to maintain most of its stars and remain bound, potentially surviving for a gigayear (e.g., Lada et al. 1984; Kroupa & Boily 2002; Bastian & Goodwin 2006; Goodwin & Bastian 2006; Baumgardt et al. 2008; Allison et al. 2010; Krause et al. 2012; Smith et al. 2013; Kim et al. 2016).

5.3. *Origin for the Velocity Gradient across the SSC*

In Section 4.2, we report a velocity gradient in the Brα core of $\simeq$2.4 km s^{-1} pc^{-1} from the NE to SW edges of the supernebula, oriented perpendicular to the NIRSPAO slits. We suggest the following possible explanations for this feature: bulk rotation of the cluster, an outflow from an embedded source in the cluster, or a foreground infalling gas filament.

5.3.1. *Rotation of the SSC*

Stellar dynamical studies of Galactic GCs have revealed that bulk rotation is common among the population (e.g., Kamann et al. 2018). These investigations find evidence for a correlation between the rotation and mass of GCs, consistent with a scenario in which a forming GC inherits angular momentum from its collapsing parent molecular cloud. Simulations of massive-cluster formation agree with this picture, finding rotation in newborn clusters (e.g., Lee & Hennebelle 2016; Mapelli 2017). Direct dynamical evidence for rotation exists for a handful of YMCs. For example, R136 within the LMC exhibits a typical rotation velocity of $\sim$3 km s^{-1} based on stars within a radius of 10 pc (Hénault-Brunet et al. 2012). A velocity gradient of $\sim$1 km s^{-1} pc^{-1} is found for the stellar surface population in the Galactic star-forming region L1688 (Rigliaco et al. 2016).

The magnitude of the Brα shift across the supernebula is similar to those measured in YMCs for which rotation is suggested. However, the mass of the SSC in NGC 5253 is orders of magnitude larger than that of such YMCs (which have $M \lesssim 10^4\,M_\odot$). The formation mechanism of SSCs is likely to differ from that of Galactic YMCs, along with the details by which angular momentum of the parent cloud is imprinted on the cluster as rotation. The CO(3–2) line, associated with hot cores and individual forming stars within the cluster, may show a slight systematic shift in its spatial centroid across the line, in the same sense as the Brα, with the bluer side of the line shifted about 0.″07 to the north of the red side of the line.

5.3.2. *A Bipolar Ionized Outflow*

The Brα gradient could alternatively provide evidence for a bipolar outflow oriented along the NE–SW axis. The implied outflow is slow, traveling at a projected speed of $\sim 10\,\mathrm{km\,s^{-1}}$, likely with a true velocity of up to a few tens of $\mathrm{km\,s^{-1}}$. Bipolar ionized outflows are commonly observed around other massive protoclusters, and can be caused by a the breaking out of winds from an embedded source, such as a massive protostellar object with an accretion disk, or a star escaping from the cluster. The outflow could even be a supernova remnant that has punched through a low density channel in the SSC.

A similar ionized outflow is observed around the IRS2 protocluster in the Galactic star-forming region W51 (Lacy et al. 2007; Ginsburg et al. 2016). The implied mass-loss rate from this cluster is $\lesssim 10^{-3}\,M_{\odot}\,\mathrm{yr}^{-1}$. NGC 5253 is an order of magnitude more massive than IRS2 and has an escape velocity that is correspondingly larger. At the same mass-loss rate, only $\sim$2% of the $\sim$60,000 $M_{\odot}$ of gas in Cloud D1 would escape from the SSC over 1 Myr. Thus, the potential bipolar outflow is likely negligible in suppressing star formation, but could provide another channel through which the SSC enriches its environment.

5.3.3. A Foreground Redshifted Gas Filament

The nuclear starburst in NGC 5253 is thought to be fueled by infalling filaments of cold gas along the galaxy's minor axis, as suggested by redshifted CO clouds (Meier et al. 2002; Turner et al. 2015). There are a number of filamentary CO(3–2) clouds detected within the starburst region that might provide a channel for gas to flow into the center of the galaxy and fuel formation of the SSC (Consiglio et al. 2017; Turner et al. 2017). Most intriguing is Cloud D4, identified in Consiglio et al. (2017). Located $\sim$10–20 pc to the south of Cloud D1 and the supernebula, Cloud D4 hosts no obvious star formation, is $\sim 3\times$ more massive than Cloud D1, and is redshifted from it by $\sim$15–20 $\mathrm{km\,s^{-1}}$. As is apparent in Figure 3, the CO(3–2) emission forms a bridge between clouds D1 and D4, suggesting that gas in the clouds are physically connected and gas could be accreting into Cloud D1 from Cloud D4.

The velocity gradient of Brα, redshifted in the SW relative to the NE, could be linked to infalling gas from cloud D4. In this scenario, the Brα originates in gas ionized by the SSC as it flows from D4 to D1. The velocity structure might be due entirely to the gas inflow, although outflow from mechanical feedback in the NE might still exist. Unfortunately, our NIRSPAO slits do not cover any positions to the south of the supernebula. Sensitive mapping of Brα across the region joining clouds D1 and D4, and around the other CO(3–2) clouds nearby, is necessary to provide more direct evidence of cold filament accretion.

6. Summary

We have obtained 0$''$.1 resolution NIRSPAO observations of the Brα 4.05 μm recombination line of the supernebula in NGC 5253, one of the most promising candidates for a young GC. Our echelle spectra ($R \sim 25{,}000$) taken with laser-guided AO on Keck II in four slit positions across the nebula allow for a detailed investigation of ionized gas kinematics in the region. Our findings are the following.

1. The K-band continuum peak is found to be coincident with the Brα peak within $\lesssim$0$''$.035, or 0.6 pc. Thus the 2 μm continuum is coincident with radio free–free emission, the "supernebula" along with the molecular Cloud D1 (Turner et al. 2017). The peak lies in a region of high visible extinction, and we suggest that it is hot dust emission.
2. The visible nuclear SSC candidates #5 and #11 (Calzetti et al. 2015), are offset from the supernebula by 0$''$.35 (6 pc) and 0$''$.14 (2.6 pc), respectively. Given their separation, these sources are unlikely to power the luminous H II region. Cluster #5 coincides with a weak, secondary K-band peak.
3. The NIRSPAO spectra of the supernebula contain strong Brα emission, and He I 4.049 μm emission that is $\sim 15\times$ weaker. The Brα line exhibits a small core linewidth of $\mathrm{FWHM_{core}} = 65$–$76\,\mathrm{km\,s^{-1}}$. The profile is consistent with a collection of individual (nonoverlapping) compact H II regions, embedded within the cluster and moving according to its gravitational potential.
4. A weak, broad pedestal is detected on the base of the Brα line, with a linewidth of $\mathrm{FWHM_{wing}} \simeq 150$–$175\,\mathrm{km\,s^{-1}}$. This feature could trace a population of massive stars expelling high-velocity winds that can escape the SSC.
5. The Brα emission is extended to the east of the supernebula, near cluster #5, and is redshifted by $\simeq$5–15 $\mathrm{km\,s^{-1}}$ with respect to the eastern edge of the supernebula. The extended gas is likely foreground to the supernebula and falling toward it. It remains unclear whether cluster #5 is indeed a star cluster that is in the process of merging with the central SSC, or a dense knot of gas/dust that reflects the visible light of the embedded cluster and may be enriched with material expelled from the SSC.
6. The centroids of the narrow Brα component and the He I doublet exhibit a velocity shift of $+13\,\mathrm{km\,s^{-1}}$ from the northeast to southwest edge of the supernebula. A similar velocity shift of smaller magnitude is seen in CO. The velocity profile is inconsistent with spherical expansion/outflow, but could be due to rotation along the axis parallel to the slits, a bipolar outflow from an embedded source driving a wind breaking out of the cluster with a velocity of $\sim$10–50 $\mathrm{km\,s^{-1}}$, or accretion of gas from a massive, redshifted cloud to the south of Cloud D1.

We suggest that we see in the supernebula/Cloud D1 region the dynamics of individual ultra-compact H II regions around massive stars within the giant cluster that powers the supernebula. Winds and supernovae from these massive stars may be stalled due to critical radiative cooling, and cannot merge to generate a cluster-scale superwind. We detect two possible sources of outflow: the broad component of Brα along with the velocity gradient of the narrow component across the supernebula. Neither of these appear to be presently capable of rapidly removing a large amount of gas from the SSC. While NGC 5253 has been thoroughly studied, its context in the general formation of massive clusters (such as GCs) remains unclear. Is the embedded SSC unique in its lack of high-velocity gas dispersal, or is it typical of SSCs of a given mass along their evolutionary paths? Further high-resolution, infrared spectroscopic studies of forming massive clusters can probe ionized gas to subcluster scales and peer past the veil of dust in which the stars of a young cluster are embedded.

The data presented herein were obtained at the W. M. Keck Observatory, which is operated as a scientific partnership among the California Institute of Technology, the University of California, and the National Aeronautics and Space Administration. The observatory was made possible by the generous financial support of the W. M. Keck Foundation. The authors wish to recognize and acknowledge the very significant cultural role and reverence that the summit of Maunakea has always had within the indigenous Hawaiian community. We are most fortunate to have the opportunity to conduct observations from this mountain. Additional support is provided by the NSF through grant AST 1515570 to J. L. Turner. The authors thank S. Silich (Instituto Nacional de Astrofísica, Óptica y Electrónica) and the anonymous referee for valuable discussion and recommendations for the manuscript.

Facility: Keck:II (NIRSPAO).

Software: IRAF, SAOImage DS9, Astropy (Astropy Collaboration et al. 2013).

ORCID iDs

Daniel P. Cohen https://orcid.org/0000-0002-5221-2342
Jean L. Turner https://orcid.org/0000-0003-4625-2951
S. Michelle Consiglio https://orcid.org/0000-0002-0214-0491
Emily C. Martin https://orcid.org/0000-0002-0618-5128
Sara C. Beck https://orcid.org/0000-0002-5770-8494

References

Allison, R. J., Goodwin, S. P., Parker, R. J., Portegies Zwart, S. F., & de Grijs, R. 2010, MNRAS, 407, 1098
Alonso-Herrero, A., Takagi, T., Baker, A. J., et al. 2004, ApJ, 612, 222
Astropy Collaboration, Robitaille, T. P., Tollerud, E. J., et al. 2013, A&A, 558, A33
Bastian, N., & Goodwin, S. P. 2006, MNRAS, 369, L9
Baumgardt, H., Kroupa, P., & Parmentier, G. 2008, MNRAS, 384, 1231
Beck, S. C. 2008, A&A, 489, 567
Beck, S. C., Lacy, J. H., Turner, J. L., et al. 2012, ApJ, 755, 59
Beck, S. C., Turner, J. L., Ho, P. T. P., Lacy, J. H., & Kelly, D. M. 1996, ApJ, 457, 610
Bendo, G. J., Miura, R. E., Espada, D., et al. 2017, MNRAS, 472, 1239
Bolatto, A. D., Warren, S. R., Leroy, A. K., et al. 2013, Natur, 499, 450
Calzetti, D., Meurer, G. R., Bohlin, R. C., et al. 1997, AJ, 114, 1834
Calzetti, D., Johnson, K. E., Adamo, A., et al. 2015, ApJ, 811, 75
Cantó, J., Raga, A. C., & Rodríguez, L. F. 2000, ApJ, 536, 896
Chevalier, R. A., & Clegg, A. W. 1985, Natur, 317, 44
Consiglio, S. M., Turner, J. L., Beck, S., & Meier, D. S. 2016, ApJL, 833, L6
Consiglio, S. M., Turner, J. L., Beck, S., et al. 2017, ApJ, 850, 54
Conti, P. S. 1991, ApJ, 377, 115
Cresci, G., Vanzi, L., Sauvage, M., Santangelo, G., & van der Werf, P. 2010, A&A, 520, A82
de Grijs, R., Anders, P., Zackrisson, E., & Östlin, G. 2013, MNRAS, 431, 2917
De Pree, C. G., Wilner, D. J., & Goss, W. M. 2011, AJ, 142, 177
De Pree, C. G., Wilner, D. J., Goss, W. M., Welch, W. J., & McGrath, E. 2000, ApJ, 540, 308
De Pree, C. G., Wilner, D. J., Mercer, A. J., et al. 2004, ApJ, 600, 286
Dreher, J. W., Johnston, K. J., Welch, W. J., & Walker, R. C. 1984, ApJ, 283, 632
Dyson, J. E., Williams, R. J. R., & Redman, M. P. 1995, MNRAS, 277, 700
Ginsburg, A., Goss, W. M., Goddi, C., et al. 2016, A&A, 595, A27
Goodwin, S. P., & Bastian, N. 2006, MNRAS, 373, 752
Hamann, F., & Simon, M. 1986, ApJ, 311, 909
Hénault-Brunet, V., Gieles, M., Evans, C. J., et al. 2012, A&A, 545, L1
Henry, A. L., Turner, J. L., Beck, S. C., Crosthwaite, L. P., & Meier, D. S. 2007, AJ, 133, 757
Hollenbach, D., Johnstone, D., Lizano, S., & Shu, F. 1994, ApJ, 428, 654
Hunt, L., Bianchi, S., & Maiolino, R. 2005, A&A, 434, 849
Jaffe, D. T., & Martín-Pintado, J. 1999, ApJ, 520, 162
Kamann, S., Husser, T.-O., Dreizler, S., et al. 2018, MNRAS, 473, 5591
Kim, J.-G., Kim, W.-T., & Ostriker, E. C. 2016, ApJ, 819, 137
Kobulnicky, H. A., Skillman, E. D., Roy, J.-R., Walsh, J. R., & Rosa, M. R. 1997, ApJ, 477, 679
Krause, M., Charbonnel, C., Decressin, T., et al. 2012, A&A, 546, L5
Kroupa, P., & Boily, C. M. 2002, MNRAS, 336, 1188
Kroupa, P., Weidner, C., Pflamm-Altenburg, J., et al. 2013, in The Stellar and Sub-Stellar Initial Mass Function of Simple and Composite Populations, ed. T. D. Oswalt & G. Gilmore (Dordrecht: Springer), 115
Lacy, J. H., Jaffe, D. T., Zhu, Q., et al. 2007, ApJL, 658, L45
Lada, C. J., Margulis, M., & Dearborn, D. 1984, ApJ, 285, 141
Lamers, H. J. G. L. M., & Cassinelli, J. P. 1999, Introduction to Stellar Winds (Cambridge: Cambridge Univ. Press)
Lee, Y.-N., & Hennebelle, P. 2016, A&A, 591, A30
Lizano, S., Canto, J., Garay, G., & Hollenbach, D. 1996, ApJ, 468, 739
López-Sánchez, Á. R., Esteban, C., García-Rojas, J., Peimbert, M., & Rodríguez, M. 2007, ApJ, 656, 168
Mapelli, M. 2017, MNRAS, 467, 3255
Martín-Hernández, N. L., Schaerer, D., & Sauvage, M. 2005, A&A, 429, 449
Matzner, C. D. 2002, ApJ, 566, 302
McLean, I. S., Becklin, E. E., Bendiksen, O., et al. 1998, Proc. SPIE, 3354, 566
Meier, D. S., Turner, J. L., & Beck, S. C. 2002, AJ, 124, 877
Monreal-Ibero, A., Vílchez, J. M., Walsh, J. R., & Muñoz-Tuñón, C. 2010, A&A, 517, A27
Oey, M. S., Herrera, C. N., Silich, S., et al. 2017, ApJL, 849, L1
Persson, S. E., Geballe, T. R., McGregor, P. J., Edwards, S., & Lonsdale, C. J. 1984, ApJ, 286, 289
Piotto, G., Milone, A. P., Bedin, L. R., et al. 2015, AJ, 149, 91
Renzini, A. 2013, MmSAI, 84, 162
Rigliaco, E., Wilking, B., Meyer, M. R., et al. 2016, A&A, 588, A123
Rodríguez-Rico, C. A., Goss, W. M., Turner, J. L., & Gómez, Y. 2007, ApJ, 670, 295
Sakai, S., Ferrarese, L., Kennicutt, R. C., Jr., & Saha, A. 2004, ApJ, 608, 42
Sakamoto, K., Ho, P. T. P., Iono, D., et al. 2006, ApJ, 636, 685
Schaerer, D., Contini, T., Kunth, D., & Meynet, G. 1997, ApJL, 481, L75
Sewilo, M., Churchwell, E., Kurtz, S., Goss, W. M., & Hofner, P. 2004, ApJ, 605, 285
Silich, S., & Tenorio-Tagle, G. 2017, MNRAS, 465, 1375
Silich, S., & Tenorio-Tagle, G. 2018, MNRAS, in press (arXiv:1805.09444)
Silich, S., Tenorio-Tagle, G., & Muñoz-Tuñón, C. 2003, ApJ, 590, 791
Silich, S., Tenorio-Tagle, G., & Rodríguez-González, A. 2004, ApJ, 610, 226
Smith, L. J., Crowther, P. A., Calzetti, D., & Sidoli, F. 2016, ApJ, 823, 38
Smith, R., Goodwin, S., Fellhauer, M., & Assmann, P. 2013, MNRAS, 428, 1303
Tenorio-Tagle, G. 1979, A&A, 71, 59
Tenorio-Tagle, G., Muñoz-Tuñón, C., Silich, S., & Cassisi, S. 2015, ApJL, 814, L8
Tenorio-Tagle, G., Silich, S., Martínez-González, S., et al. 2013, ApJ, 778, 159
Tokunaga, A. T. 2000, in Allen's Astrophysical Quantities, ed. A. N. Cox (4th ed.; New York: Springer), 143
Turner, J. L. 2009, in Astrophysics in the Next Decade: JWST and Concurrent Facilities, ed. H. A. Thronson et al. (Berlin: Springer), 215
Turner, J. L., & Beck, S. C. 2004, ApJL, 602, L85
Turner, J. L., Beck, S. C., Benford, D. J., et al. 2015, Natur, 519, 331
Turner, J. L., Beck, S. C., Crosthwaite, L. P., et al. 2003, Natur, 423, 621
Turner, J. L., Beck, S. C., & Ho, P. T. P. 2000, ApJL, 532, L109
Turner, J. L., Consiglio, S. M., Beck, S. C., et al. 2017, ApJ, 846, 73
Turner, J. L., Ho, P. T. P., & Beck, S. C. 1998, AJ, 116, 1212
Vanzi, L., & Sauvage, M. 2004, A&A, 415, 509
Walsh, J. R., & Roy, J.-R. 1989, MNRAS, 239, 297
Westmoquette, M. S., James, B., Monreal-Ibero, A., & Walsh, J. R. 2013, A&A, 550, A88
Wood, D. O. S., & Churchwell, E. 1989, ApJS, 69, 831
Wünsch, R., Palouš, J., Tenorio-Tagle, G., & Ehlerová, S. 2017, ApJ, 835, 60